

# Integrated Machine-learning Force Prediction Model of H-shaped Steel during Hot-rolling Manufacturing with Measurements via Sensors

Long Wu,<sup>1</sup> De-Yu Zang,<sup>1</sup> Kun-Chieh Wang,<sup>1\*</sup> Si-Jie Qiu,<sup>1</sup> and Jian-Zhou Pan<sup>2</sup>

<sup>1</sup>School of Mechanical and Electric Engineering, Sanming University, Sanming, Fujian Province 365004, China

<sup>2</sup>Fujian Sansteel (Group) Co., Ltd., Sanming, Fujian 365000, China

(Received January 27, 2025; accepted May 13, 2025)

**Keywords:** H-shaped steel, rolling force prediction model, bar beam steel, hot-rolling process, machine learning

In this study, we introduce an optimal rolling force prediction model for H-shaped steel during the hot-rolling process, employing multiple machine learning methods. The traditional rolling force prediction model often relies on simplistic empirical formulas that fail to account for the complex and variable shape of H-shaped steel, leading to potential product defects. To address this limitation and enhance the effectiveness of traditional prediction models, we propose a novel integrated machine learning approach, the Particle Swarm Optimization-Least Squares Support Vector Machine-AdaBoost (PSO-LSSVM-A) model, for predicting the optimal rolling force applied during the hot rolling of H-shaped steel. Initially, the geometric and physical parameters of H-shaped steel during the hot-rolling process are acquired through sensor-based experimental measurements. To ensure data integrity, the Isolation Forest (IForest) algorithm is employed to identify and eliminate outliers. Subsequently, the PSO algorithm is utilized to optimize the calculation parameters involved in the LSSVM modeling process. Finally, the adaptive AdaBoost algorithm, combined with a weight allocation scheme, is integrated to further enhance the prediction effectiveness of the overall model. Through comparisons, we found that the proposed PSO-LSSVM-A model exhibits superior accuracy and stability in predicting the rolling force of H-shaped steel webs during the hot-rolling manufacturing process. The proposed PSO-LSSVM-A model not only considers the intricate geometry and physical characteristics of H-shaped steel but also leverages the optimization capabilities of the PSO algorithm and the ensemble learning power of the AdaBoost algorithm to deliver robust and reliable predictions. By bridging the gap between traditional empirical and advanced machine learning methods, we developed the model representing a significant advancement in optimizing the hot-rolling process for H-shaped steel, ultimately leading to enhanced productivity and product quality, and extended product life in the manufacturing industry.

---

\*Corresponding author: e-mail: [m18316252102@126.com](mailto:m18316252102@126.com)  
<https://doi.org/10.18494/SAM5569>

## 1. Introduction

In the realm of metalworking, the process of beam or bar rolling stands as a cornerstone, facilitating the transformation of raw materials into a myriad of essential products across industries. Essential to this process is the prediction and control of beam or bar rolling forces, a fundamental parameter governing the efficiency, quality, and safety of operation.<sup>(1–5)</sup> The complexities inherent in bar rolling, stemming from material properties, equipment dynamics, and process variables, necessitate sophisticated predictive models to optimize performance and mitigate risks.

The prediction of bar rolling forces has attracted significant attention within the metallurgical and engineering communities owing to its direct impact on product quality, energy consumption, and equipment longevity. Understanding and controlling these forces enable manufacturers to enhance productivity, reduce material waste, and ensure the structural integrity of rolled products. Consequently, the development of accurate and reliable prediction models for bar rolling forces emerges as a critical endeavor, underpinning advancements in the field of metal forming and manufacturing.<sup>(6,7)</sup>

Historically, the prediction of rolling forces relied on empirical approaches, leveraging past data and heuristic relationships to estimate the forces exerted during the rolling process. While effective to some extent, these methods often lacked the capability to capture the intricacies of the rolling process, leading to suboptimal performance and limited predictive accuracy. With the advent of computational techniques and advancements in materials science, there has been a paradigm shift towards the development of physics-based models, grounded in the fundamental principles of mechanics and material behavior.

Physics-based approaches offer a more comprehensive understanding of the underlying phenomena governing bar rolling, taking into account factors such as material properties, frictional effects, and deformation characteristics. By incorporating principles from continuum mechanics, thermodynamics, and tribology to these approaches, we can simulate the intricate interplay among the rolling mill components, the workpiece, and the surrounding environment. Through numerical simulations and finite element analysis, researchers aim to elucidate the complex interactions occurring at the microstructural level, thereby enabling more accurate predictions of rolling forces.<sup>(8,9)</sup>

Key challenges in the development of bar rolling force prediction models revolve around the inherent nonlinearity and variability of the process. The dynamic nature of rolling operations, coupled with uncertainties in material properties and operating conditions, poses significant obstacles to modeling fidelity and robustness.<sup>(10,11)</sup>

To address these challenges, researchers employ a diverse array of modeling techniques, ranging from analytical formulations to numerical simulations and machine learning (ML) methods.<sup>(12–14)</sup> Analytical models, grounded in classical theories of solid mechanics and plasticity, offer insights into the fundamental mechanisms governing deformation and stress distribution during rolling.<sup>(15,16)</sup> However, their applicability is often limited to idealized geometries and simplified assumptions, necessitating validation against experimental data for real-world relevance.

Numerical simulations, on the other hand, provide a more versatile platform for modeling complex rolling processes, allowing for the incorporation of geometric complexities, material heterogeneities, and boundary conditions.<sup>(17)</sup> Finite element analysis serves as a cornerstone in this regard, enabling researchers to discretize the rolling mill system into finite elements and solve for the governing equations of motion under various loading conditions.

In recent years, the ML method has emerged as a powerful tool for data-driven modeling and prediction in the field of bar rolling.<sup>(18–20)</sup> By leveraging vast amounts of historical data on process parameters, material properties, and rolling outcomes in ML methods, we can identify complex patterns and correlations that elude traditional analytical and numerical approaches. Neural networks, support vector machines (SVMs), and ensemble methods offer flexible frameworks for building predictive models that can adapt to evolving process conditions and learn from past experiences.<sup>(21)</sup> Despite their promise, however, ML methods face challenges related to data quality, feature selection, and generalization to unseen scenarios.<sup>(22,23)</sup> The curses of dimensionality, overfitting, and bias in training data can compromise the reliability and robustness of ML-based predictions, necessitating careful validation and model selection procedures.<sup>(24,25)</sup> Moreover, the interpretability of black-box models remains a concern, as stakeholders often require insights into the underlying mechanisms driving the predictions for informed decision-making. Previous research on ML methods for rolling force prediction has primarily concentrated on steel strip rolling. However, there has been little scholarly attention on predicting the rolling force of H-shaped steel over the past decade, particularly using advanced techniques such as ML or deep learning neural networks.

To address this issue, in this study, we propose an innovative integrated ML model: the Particle Swarm Optimization-Least Squares Support Vector Machine-AdaBoost (PSO-LSSVM-A) model. It is designed for achieving high prediction accuracy and fast convergence in predicting the rolling force of H-shaped steel.

## 2. Theoretical Foundation

Our proposed PSO-LSSVM-A model integrates multiple ML methods, including the Isolation Forest (IForest) algorithm, PSO algorithm, and LSSVM method. Additionally, we incorporate the AdaBoost algorithm to further enhance the model's efficiency and accuracy, resulting in a novel PSO-LSSVM-A model. A detailed description of the PSO-LSSVM-A model is provided below.

### 2.1 IForest algorithm for outlier detection

The IForest algorithm is an ML method designed for outlier detection.<sup>(26)</sup> It is well suited for analyzing continuous and complex datasets, known for its efficiency and accuracy in outlier detection. This algorithm consists of several independently constructed isolated trees and aims to identify outliers through the framework of random forests. In building each isolated tree, the algorithm randomly selects a feature dimension and a segmentation value within that dimension's range. This divides the dataset into two subsets. This splitting process is repeated recursively

until specific termination conditions are met. The core idea behind the algorithm is that abnormal data points are likely to be isolated early in the segmentation process because of their rarity, resulting in relatively short paths within the tree structure. The steps to build a single tree are as follows:

- (1) Randomly select a subsample of  $\beta$  data points from the entire dataset.
- (2) Randomly select a feature from all the features available in the subsample.
- (3) Randomly choose a split point by selecting a value between the minimum and maximum of the chosen feature.
- (4) Divide the data into two subsets on the basis of the split point:  
One subset contains all points where the feature value is less than or equal to the split point value.  
The other subset contains points where the feature value is greater than the split point value.
- (5) Recursively repeat steps 2 to 4 on each of the resulting subsets until either the subset size falls below a predefined threshold or the tree reaches a specified maximum depth.

The above steps are repeated  $t$  times to obtain  $t$  isolated trees and generate an isolated forest. All data sample points are included, and the anomaly score is calculated using Eqs. (1)–(3) as follows.

$$s(x, \beta) = 2^{\frac{-E(h(x))}{c(\beta)}}, \quad (1)$$

$$c(\beta) = 2H(\beta - 1) - (2(\beta - 1) / \beta), \quad (2)$$

$$H(*) = \ln(*) + \xi, \quad (3)$$

where  $E(h(x))$  is the expected value of the path length of  $x$  in multiple trees,  $c(\beta)$  is the average path length of a dataset containing  $\beta$  samples, used to standardize the path length of the record,  $H(*)$  is a harmonic function, and  $\xi$  is the Euler's constant with a value of about 0.577.<sup>(26)</sup> We used the IForest algorithm to detect data anomalies. The IForest algorithm identified 5% of the data as outliers. For the H-shaped steel data analyzed in this study, the IForest algorithm identified 5% of the outliers. The results are depicted in Fig. 1, where red points indicate outliers, blue points denote normal values, and the horizontal and vertical coordinates represent the data points' positions in the selected feature space, without a specific "unit" assigned.

## 2.2 LSSVM scheme as kernel model

The SVM is an ML method proposed by Vapnik<sup>(26)</sup> on the basis of the principle of structural risk minimization within statistical learning theory. It has been proven effective in handling learning tasks with small sample sizes, showcasing robust classification and regression capabilities as well as strong generalization capabilities. For an input data sample  $x_i$  in a training set, let  $y_i \in R$  denote its expected output. We formulate a constrained minimization problem using LSSVM as follows:

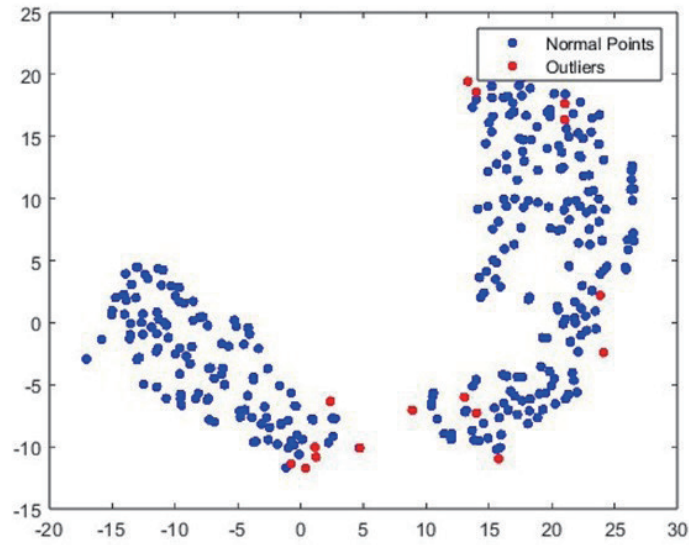


Fig. 1. (Color online) Anomaly detection using IForest algorithm.

$$\min \quad \frac{1}{2} \|w\|^2 + \frac{\lambda}{2} \sum_{i=1}^l e_i^2, \tag{5}$$

$$\text{s.t.} \quad y_i = W^T \Phi(x_i) + b + e_i, \quad i = 1, 2, \dots, l, \tag{6}$$

where  $w$  represents the weight coefficients,  $b$  denotes the threshold,  $e_i$  is the error term,  $\lambda$  is the penalty function, and  $\Phi(x_i)$  is the mapping function that transforms data from a low-dimensional space to a high-dimensional space. The loss function is introduced as

$$L(w, b, e, a_i) = \frac{1}{2} \|w\|^2 + \frac{\lambda}{2} \sum_{i=1}^l e_i^2 - \sum_{i=1}^l a_i [W^T \Phi(x_i) + b + e_i - y_i]. \tag{7}$$

Now, we linearize Eqs. (5)–(7) into the following linearization problem:

$$\begin{cases} \frac{\partial L}{\partial w} = w - \sum_{i=1}^l a_i \Phi(x_i) = 0 \rightarrow w = \sum_{i=1}^l a_i \Phi(x_i), \\ \frac{\partial L}{\partial b} = -\sum_{i=1}^l a_i = 0 \rightarrow \sum_{i=1}^l a_i = 0, \\ \frac{\partial L}{\partial e_i} = \lambda \sum_{i=1}^l e_i - \sum_{i=1}^l a_i = 0 \rightarrow a_i = \lambda e_i, \\ \frac{\partial L}{\partial a_i} = 0 \rightarrow W^T \Phi(x_i) + b + e_i - y_i = 0. \end{cases} \tag{8}$$

By further simplifying the above equation, we obtain a matrix form for calculating  $a_i$  and  $b$ :

$$\begin{pmatrix} 0 & e_1 \\ e_1^T & K + \frac{1}{\lambda} I \end{pmatrix} \begin{pmatrix} b \\ a \end{pmatrix} = \begin{pmatrix} 0 \\ y \end{pmatrix}, \quad (9)$$

where  $I \in R^l$  is a unitary matrix, and  $K$  is a kernel matrix with dimension  $l * l$ . In this study, we adopt the radial basis function<sup>(19)</sup> as the kernel function:

$$K = k(x_i, x_j) = \exp\left(-\frac{|x_i - x_j|^2}{\gamma^2}\right), \quad (10)$$

where  $\gamma$  is the kernel parameter. By solving the matrix equation of Eq. (9), we have the following final regression model:

$$f(x) = \sum_{i=1}^l a_i K(x_i, y_j) + b. \quad (11)$$

### 2.3 PSO algorithm for model optimization

The PSO algorithm, introduced by Kennedy and Eberhart in 1995,<sup>(27)</sup> is an optimization technique based on collective intelligence. It draws inspiration from the foraging behavior of bird flocks and solves optimization problems by simulating this social behavior. In the PSO algorithm, each potential solution is represented as a “particle,” and the particles “fly” through the solution space to locate the optimal solution. Compared with other optimization schemes, the PSO algorithm typically requires fewer parameters to adjust and can converge to the optimal solution more quickly. Its relative simplicity in implementation has led to its widespread use in fields such as nonlinear integer programming, function optimization, and neural network training.<sup>(21)</sup>

### 2.4 PSO-LSSVM model

To better establish the rolling force prediction model of a hot-rolled H-shaped steel, we propose a novel approach, the PSO-LSSVM-A model.

#### 2.4.1 PSO-LSSVM

First, 21 parameters listed in Table 1 are selected as input variables for the rolling force prediction model. The data are then examined for outliers using the IForest algorithm. After removing outliers, the data are processed using the LSSVM model, and model parameters are optimized with the PSO algorithm. The calculation process for the PSO-LSSVM model<sup>(22)</sup> is illustrated in Fig. 2 and discussed as follows.

Table 1  
Parameters that affect the horizontal rolling force of H-shaped steel.

No.	Parameter	No.	Parameter	No.	Parameter
1	$h_0$ : initial flange thickness	8	$b_m$ : mean web span	15	$R_v$ : beam radius in vertical rolling
2	$h_1$ : flange thickness after rolling	9	$ka$ : internal width of web	16	$R_h$ : beam radius in horizontal rolling
3	$ss_0$ : initial web thickness	10	$sh$ : web height after rolling	17	$A_f$ : cross-sectional area of beam after rolling
4	$ss_1$ : web thickness after rolling	11	$L_c$ : contact arc length	18	$L_a$ : beam length after rolling
5	$b_0$ : initial web width	12	$e$ : deformation rate of web height ( $\Delta h/h_0$ )	19	$v$ : rolling velocity
6	$b_1$ : web width after rolling	13	$\varepsilon$ : relative deformation ( $\ln(h_0/h_1)$ )	20	$Z$ : rolling time
7	$\Delta b$ : web span	14	$\lambda$ : beam deformation ratio ( $\ln(h_0/h_1)/\ln(ss_0/ss_1)$ )	21	$T$ : rolling temperature

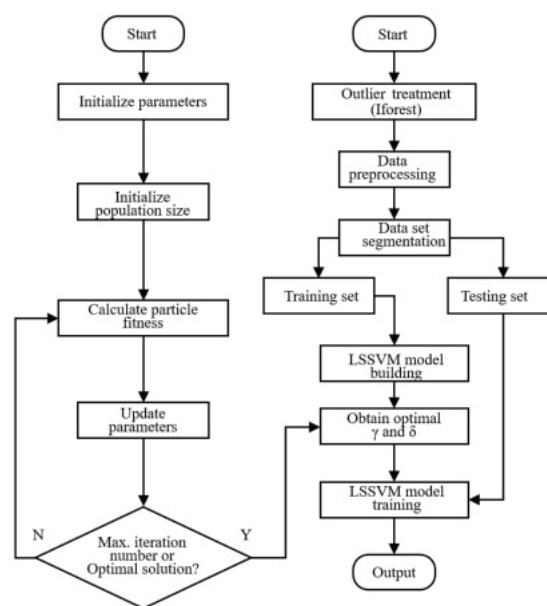


Fig. 2. Algorithm of PSO-LSSVM model.

- (1) Import the dataset, apply the IForest algorithm to remove outliers, split the dataset into training and test sets, and normalize the data.
- (2) Initialize the PSO-LSSVM model, setting the parameters as specified in Table 1.
- (3) Input the parameter combinations for each particle into the PSO-LSSVM model for training and calculate each particle's fitness value using the adaptation function.
- (4) Compare each particle's current fitness value with its historical best position. If the current value is better, update the particle's individual best solution.
- (5) Compare each particle's best fitness value with the global best position. If a particle's best position has a higher fitness value, update the global best solution.
- (6) Determine whether the maximum number of iterations has been reached or if the global optimal solution has been achieved. If either is true, output the optimal parameter combination and assign it to the LSSVM model. If not, return to step 3.
- (7) Utilize the best parameter combination to train the model on the training set and evaluate the model's performance on the test set.

(8) Inverse-normalize the predicted results from the test set to obtain the rolling force prediction outcomes.

The PSO-LSSVM model is trained with the objective of minimizing the mean square error (*MSE*), and its fitness function ( $\Omega$ ) is defined as

$$\Omega = \min \left\{ \frac{1}{N} \sum_{i=1}^N (y_i - f(x_i))^2 \right\}, \quad (12)$$

where  $y_i$  is the rolling force and  $x_i$  is the selected input parameter.

## 2.5 PSO-LSSVM-A model

To enhance the accuracy of the PSO-LSSVM model for predicting H-shaped steel rolling force, we further introduce the adaptive boosting (AdaBoost) error compensation scheme.<sup>(28)</sup> This scheme employs the weight allocation in the AdaBoost algorithm to optimize the calculation sequence, thereby reducing the overall prediction error and improving the model's performance. In this optimization process, the PSO-LSSVM method serves as the base learner, functioning as a weak regressor. During the iterative procedure, the weights are dynamically adjusted according to the prediction error of each base learner: weights are increased for base learners with smaller prediction errors, while weights are decreased for those with larger prediction errors. The calculation procedure of the PSO-LSSVM-A model is shown in Fig. 3 and depicted as follows.

- (1) Import and preprocess data: Import the data, preprocess it, and divide it into training and test sets.
- (2) Optimize LSSVM parameters: Use the PSO algorithm to optimize the parameters of the LSSVM.
- (3) Initialize and train the LSSVM scheme: Initialize the LSSVM scheme with the optimized parameters. Import the dataset and use it to train the PSO-LSSVM model.
- (4) Initialize weak regressors: Set the number of weak regressors to  $K$  and initialize the weights for the training data. Assign each sample the same weight,  $\omega_i = 1/K$ , creating the initial weight distribution  $D_1(i) = (\omega_1, \omega_2, \dots, \omega_N) = (1/K, \dots, 1/K)$  for the training samples.
- (5) Train weak regressors and update weights: For each weak regressor, train a new PSO-LSSVM model. Set the weights of each weak regressor to  $D_k(i)$ . Construct the prediction set  $h_k(x_i)$  from the PSO-LSSVM model, calculate the prediction error, adjust the sample weights, and update the weights of the weak regressors on the basis of the error.

$$\begin{cases} e_k = \sum_{i=1}^N D_k(i), i = 1, 2, 3, \dots, \\ \alpha_k = \frac{1}{2 \exp(|e_k(i)|)}, \\ D_{i+1} = \frac{D_k(i) \exp(-\alpha_k y_k(i) h_k(x_i))}{Z_k}, \end{cases} \quad (13)$$

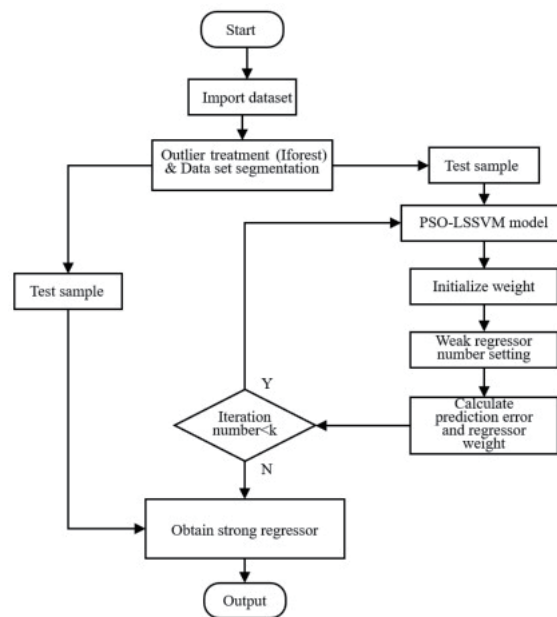


Fig. 3. Algorithm of PSO-LSSVM-A model.

where  $Z_k = 2\sqrt{e_k(1-e_k)}$  is the normalization constant,  $h_k(x_i)$  represents the predicted value of the first  $k$  subset,  $y_k(i)$  is the target value for the first subset,  $e_k$  denotes the sum of the weights of the weak regressors,  $\alpha_k$  is the weight assigned to each weak regressor in the final classifier, and  $D_{i+1}$  is the updated weight distribution of the training samples.

(6) Weight and aggregate the outputs of multiple weak regressors to form a strong regressor, combining their predictions to produce the final output:<sup>(24)</sup>

$$y(x_i) = \sum_{k=1}^k \sum_{i=1}^k \alpha_k H_k(x). \quad (14)$$

### 3. Experiments and Data Processing

#### 3.1 Experimental measurement

In this study, we focused on H-shaped steel, which consists of a web and flanges. The web deformation is affected by the magnitude of the horizontal rolling force. The rolling mill equipment for H-shaped steel includes a universal roughing mill (UR), a universal finishing mill (UF), and an edge rolling machine (E), as shown in Fig. 4. Additionally, we developed a multisensor measurement system (illustrated in Fig. 5), which incorporates infrared sensors, pressure sensors, and optical grating sensors positioned on both sides of the conveyor belt. As the H-shaped steel passes through, this system detects various physical parameters of the steel.



Fig. 4. (Color online) Manufacturing site of H-shaped steel.

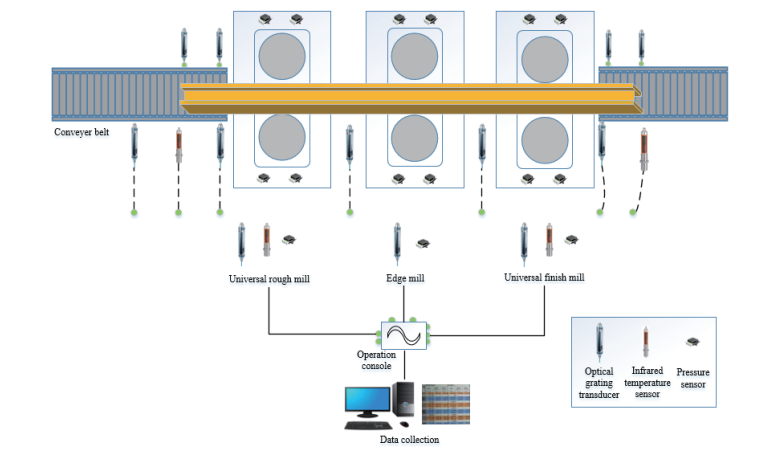


Fig. 5. (Color online) Sensor-based measurement system.

### 3.1.1 H-shaped steel parameter acquisition planning

The H-shaped steel material examined in our study is Q235. In our experiments, we gathered data on approximately 20 different sizes of H-shaped steel. The dimensions of the H-shaped billets and finished products are illustrated in Figs. 6 and 7.

We consider a total of 21 parameters that affect the horizontal rolling force ( $F$ ) of H-shaped steel during manufacturing, as listed in Table 1. Among the 21 parameters, eight parameters, namely,  $h_0$ ,  $h_1$ ,  $ss_0$ ,  $ss_1$ ,  $b_1$ ,  $ka$ ,  $R_v$ , and  $R_h$ , are directly measured using a vernier caliper (mm). The parameter  $Z$ , representing the rolling time, is measured with a timer (s). Ten parameters, namely,  $b_1$ (mm),  $\Delta b$  (mm),  $b_m$  (mm),  $sh$  (mm<sup>2</sup>),  $L_h$  (mm),  $L_v$  (mm),  $e$  (dimensionless),  $\varepsilon$  (dimensionless),  $\lambda$  (dimensionless), and  $A_t$  (mm<sup>2</sup>), are calculated from the measured data using Eqs. (15)–(29). The speed (mm/s) is measured using a grating sensor, the temperature  $T$  (°C) is

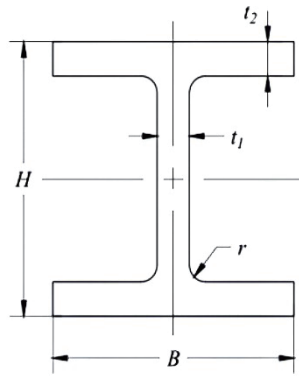


Fig. 6. H-shaped steel specifications ( $H$ : height,  $B$ : width,  $t_1$ : web thickness,  $t_2$ : flange thickness,  $r$ : radius of corner).

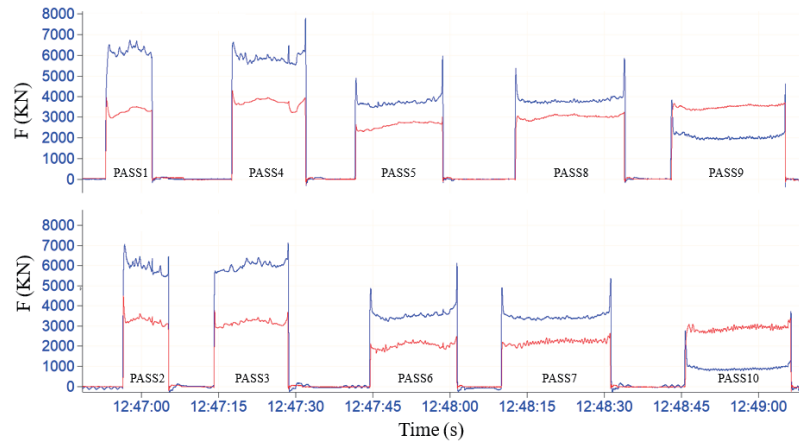


Fig. 7. (Color online) Variations of horizontal rolling force at each rolling station (Passes 1–10).

measured using an infrared sensor, and the rolling force  $F$  (N) is measured using a pressure sensor.

$$\Delta h = h_1 - h_0, \tag{15}$$

$$\Delta ss = ss_1 - ss_0, \tag{16}$$

$$L_h = \sqrt{R_h \Delta ss}, \tag{17}$$

$$L_v = \sqrt{R_v \Delta h}, \tag{18}$$

$$b_1^2 - b_0^2 = 8mL_v(h_0 - h_1) - 4m(h_0 + h_1)L_v \ln \frac{b_1}{b_0}, \tag{19}$$

$$m = \frac{1.6\mu L_v - 1.2(h_0 - h_1)}{h_0 + h_1}, \quad (20)$$

$$\mu = \alpha(1.05 - 0.0005T), \quad (21)$$

$$\Delta b = b_1 - b_0, \quad (22)$$

$$b_m = \frac{b_1 + b_0}{2}, \quad (23)$$

$$sh = ka + 2 \cdot (h_1 / \cos(\beta) - \tan(\beta) \cdot ss_1 / 2) + 0.38, \quad (24)$$

$$Ar = wr^2 \cdot (\tan((90 - \beta) / 2) - \pi / 360 \cdot (90 - \beta)), \quad (25)$$

$$A_t = sh \cdot ss_1 + 2 \cdot h_1 \cdot (b_1 - ss_1) + 4 \cdot Ar, \quad (26)$$

$$e = \frac{\Delta h}{h_0}, \quad (27)$$

$$\varepsilon = \ln\left(\frac{h_0}{h_1}\right), \quad (28)$$

$$\lambda = \frac{\ln(h_0 / h_1)}{\ln(ss_0 / ss_1)}. \quad (29)$$

In Eqs. (15)–(29),  $L_h$  and  $L_v$  represent the arc lengths of contact between the web and the flange (unit: mm);  $m$  is the coefficient representing the influence of friction on pressure;  $\mu$  is the friction coefficient;  $\alpha$  is the material factor for the type of rolled steel, which is set to 1 for steel rolls in this study;  $\beta$  is the side roll angle of the rolling mill— $5^\circ$  for UR and  $0.5^\circ$  for UF;  $wr$  is the radius of the finished corner (unit: mm). The definitions of other variables are provided in Table 1.

The H-shaped steel passes through 10 rolling stations, and the variation in horizontal rolling force over time at each station is shown in Fig. 7. The entire rolling process of the H-shaped steel is completed using five URs and five UFs. The URs, equipped with horizontal and vertical rolls, shape the workpiece into an X-shape, whereas the UFs perform the final shaping into an H-shape. This process is divided into five passes, with each pass through a mill recorded as a PASS. A workpiece that passes through both a UR PASS and a UF PASS is considered one cycle. As illustrated in Fig. 7, the workpiece undergoes a total of five cycles: the first cycle consists of UR (PASS1), followed by UF (PASS2), the second cycle involves UF (PASS3) and then UR

(PASS4), and so on, culminating with the fifth cycle of UR (PASS9), followed by UF (PASS10). The time required for each PASS varies.

On the basis of the measurement results, we obtained 319 sample data, some of which are presented in Table 2. We employed a sequential approach to divide the data, allocating the first 80% to the training set and the last 20% to the test set, following an 80:20 ratio. The training set was utilized to initially evaluate the performance of the horizontal rolling force model and to adjust its internal parameters. On the other hand, the test set was used to assess the model's accuracy and generalization capability.

### 3.2 Normalization and error estimation

We used the max–min standard normalization formula to preprocess the initial data, as follows:

$$X_i = \frac{x_i - x_{min}}{x_{max} - x_{min}}, \quad (16)$$

where  $x_i$  is the original data and  $X_i$  is the normalized data.

On the other hand, for error estimation in modeling, the error index of coefficient of determination ( $R^2$ ), mean absolute error ( $MAE$ ), and root mean square error ( $RMSE$ ) are introduced:

Table 2  
Partial measurement results of controlled parameters.

Machine	$h_0$ (mm)	$h_1$ (mm)	$ss_0$ (mm)	$ss_1$ (mm)	$b_0$ (mm)	$b_1$ (mm)	$\Delta b$ (mm)	$b_m$ (mm)	$Ka$ (mm)	$Sh$ (mm)
UR	103	74.3	42.5	36.9	224.50	234.58	10.08	229.54	374.74	521.06
UF	74.3	58.6	36.9	29.9	229.37	234.81	5.44	232.09	377.74	495.32
UF	58.6	42.6	29.9	23.3	222.37	229.89	7.52	226.13	377.74	463.32
UR	42.6	32.8	23.3	17.1	215.77	220.09	4.32	217.93	374.74	439.47
UR	32.8	26.1	17.1	16.2	209.57	212.47	2.90	211.02	374.74	426.10
UF	26.1	22.9	16.2	13.8	208.67	209.61	0.94	209.14	377.74	423.92
UF	22.9	18.2	13.8	11.9	206.27	208.59	2.32	207.43	377.74	414.52
UR	18.2	15.3	11.9	10.2	204.37	205.49	1.12	204.93	374.74	404.94
UR	15.3	13.3	10.2	9.4	202.67	203.33	0.66	203.00	374.74	401.00
UF	13.3	12.5	9.4	8.6	201.87	202.00	0.13	201.93	377.74	404.38

$L_c$ (mm)	$e$	$\varepsilon$	$\lambda$	$R_v$ (mm)	$R_h$ (mm)	$A_t$ (mm <sup>2</sup> )	$L_a$ (mm)	$V$ (m/s)	$Z$ (s)	$T$ (°C)	$F$ (KN)
111.81	0.279	0.327	2.115	429.58	1215.6	48720.8	25.37	5.09	7.13	1096.9	7411.2
84.43	0.211	0.237	1.114	442.35	1225.5	38970.9	31.72	6.42	10.29	1091.7	6783.6
85.23	0.273	0.319	1.237	442.35	1225.5	28542.3	43.31	5.45	10.2	1085.5	6210
65.34	0.230	0.261	0.865	446.13	1215.6	20949.4	59.01	7.37	13.48	1075.2	5578.1
54.02	0.204	0.228	3.881	429.58	1215.6	17266.3	71.59	5.73	14.89	1060.3	3162.7
38.19	0.123	0.131	0.828	442.35	1225.5	14963.5	82.61	6.66	17.82	1042.4	3418.9
46.2	0.205	0.230	1.491	442.35	1225.5	12237.3	101.01	6.1	19.05	1021.5	3235.1
35.542	0.159	0.174	1.115	446.13	1215.6	10224.3	120.90	7.24	22.21	995.43	2857.9
29.516	0.131	0.140	1.667	429.58	1215.6	9045.8	136.65	6.37	24.07	965.70	1140.9
19.059	0.060	0.062	0.707	442.35	1225.5	8504.8	145.35	6.83	26.53	934.21	642.80

$$R^2 = 1 - \frac{\sum_i (y - y_i)^2}{\sum_i (\bar{y} - y_i)^2}, \quad (17)$$

$$MAE = \frac{1}{n} \sum_{i=1}^n |\bar{y} - y_i|, \quad (18)$$

$$RMSE = \sqrt{\frac{1}{m} \sum_{i=1}^m (y - y_i)^2}, \quad (19)$$

where  $\bar{y}$  is the mean value of sample data,  $y_i$  is the predicted value of sample data, and  $y$  is the real target value of sample data.

## 4. Results and Discussion

### 4.1 Comparison of measured and predicted rolling forces based on training data

For verification, 242 samples from the training dataset were selected to evaluate the proposed PSO-LSSVM-A model. The results were then compared with the measured values, as shown in Fig. 8.

In Fig. 8, the blue line represents the measured rolling force values, whereas the red line shows the predicted rolling forces generated by the PSO-LSSVM-A model. The maximum measured rolling force is 8478.66 kN, and the minimum is 857.62 kN. After training, the predicted data from the PSO-LSSVM-A model aligns closely with the actual measurements. The  $R^2$  value of 0.994, which is close to 1, indicates that the prediction model effectively explains the variation in the measured data. Additionally, the  $RMSE$  of 138.65 suggests that the average error between the predicted and actual values is small, demonstrating the model's accuracy.

Additionally, the average relative error between the measured and predicted rolling force values is 3.86%, further indicating a strong agreement between the two. Observing the blue and red lines in Fig. 8 reveals that the predicted and measured rolling force values are closely aligned in most instances, highlighting the high stability of our prediction model. Overall, the PSO-LSSVM-A model demonstrates excellent performance on the training data, showcasing both high prediction accuracy and stability.

### 4.2 Comparison of measured and predicted rolling forces based on test data

For verification, 60 samples from the test dataset were selected to evaluate the proposed PSO-LSSVM-A model. The results were then compared with the measured values, as shown in Fig. 9.

In Fig. 9, the blue line represents the measured rolling force values, whereas the red line shows the predicted rolling forces generated by the PSO-LSSVM-A model. The maximum measured rolling force is 7681.33 kN, and the minimum is 886 kN. The predicted data from the PSO-LSSVM-A model closely aligns with the actual measurements. The  $R^2$  value of 0.963

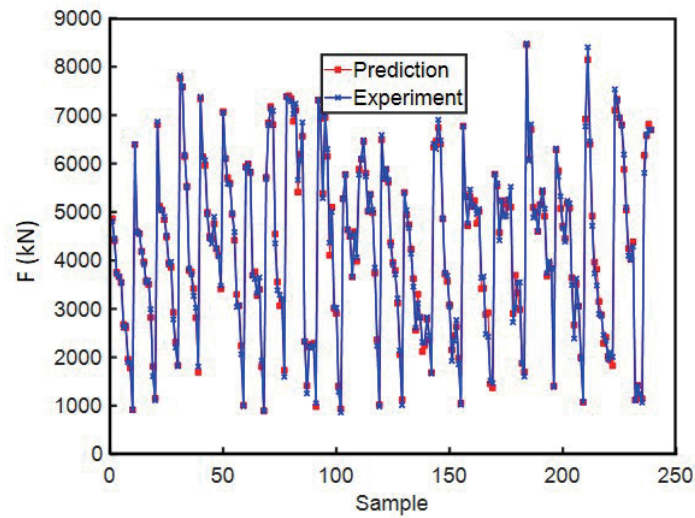


Fig. 8. (Color online) Comparison between predicted rolling force (PSO-LSSVM-A model) and measured rolling forces for the training data.

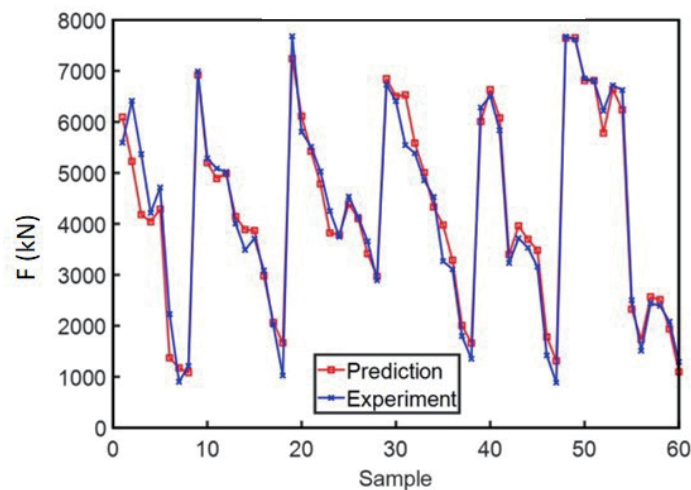


Fig. 9. (Color online) Comparison between predicted rolling force (PSO-LSSVM-A model) and measured rolling force for the test data.

indicates that the model effectively explains the variation in the measured data. Additionally, the *RMSE* value of 373.471 suggests that the average error between the predicted and actual values is low, demonstrating the model's accuracy in testing.

Although some data points, such as those for the second and third samples, exhibit significant errors of 18.49 and 22.13%, respectively, the overall average error is 8.72%, which is below 10%. This indicates that the model's prediction performance remains strong overall. Observing the blue and red lines in Fig. 9 reveals that the predicted and measured rolling force values are closely aligned in most instances, highlighting the high stability of our prediction model.

Overall, the PSO-LSSVM-A model demonstrates excellent performance on the test data, showcasing both high prediction accuracy and stability.

#### 4.3 Correlation between measured and predicted rolling forces based on training data

To understand the correlation between the predicted rolling force values from the PSO-LSSVM-A model based on training data and the actual measured values, we created a correlation scatter plot of these values, as shown in Fig. 10. In this figure, the horizontal axis represents the actual measured rolling force, whereas the vertical axis represents the predicted rolling force. The data points are roughly distributed along a straight line, indicating a strong linear relationship between the predicted and actual values, which is further confirmed by the red fitted line. The  $R^2$  value of 0.994, close to 1, indicates that the model effectively explains the variation in the actual measured data. The  $RMSE$  value of 138.651 suggests that the model has a small prediction error. Although some data points deviate from the fitted line, the measured and predicted values fit well overall.

#### 4.4 Correlation between measured and predicted rolling forces based on test data

To understand the correlation between the predicted rolling force values from the PSO-LSSVM-A model based on test data and the actual measured values, we created a correlation scatter plot of these values, as shown in Fig. 11. In this figure, the horizontal axis represents the actual measured rolling force, whereas the vertical axis represents the predicted rolling force. The data points are roughly distributed along a straight line, indicating a strong linear relationship between the predicted and actual values, which is further confirmed by the red fitted line. The  $R^2$  value of 0.963 indicates that the model effectively explains the variation in the actual measured values. The  $RMSE$  value of 373.471 suggests that the model has a small

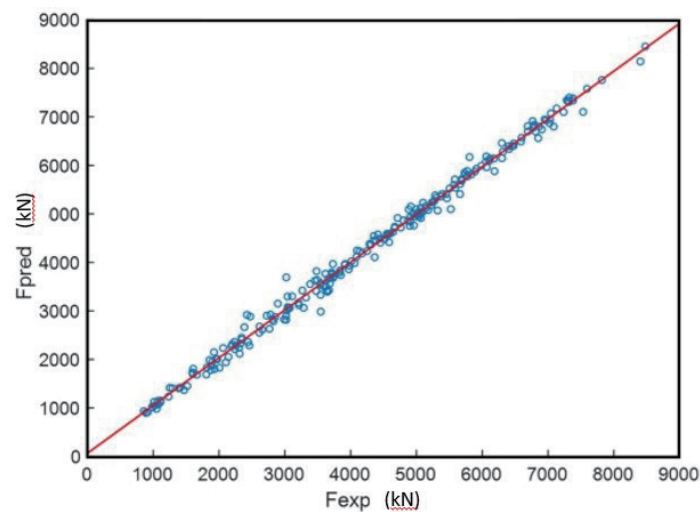


Fig. 10. (Color online) Correlation between measured and predicted rolling forces based on training data.

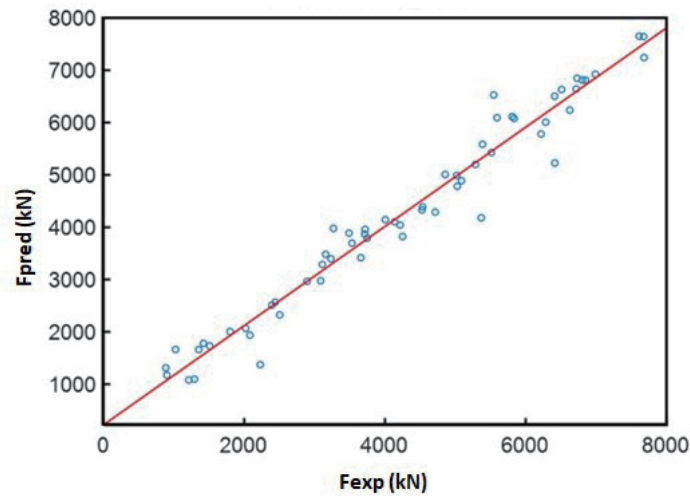


Fig. 11. (Color online) Correlation between measured and predicted rolling forces based on test data.

prediction error. Although some data points deviate from the fitted line, the measured and predicted values fit well overall.

#### 4.5 Comparison of measured and predicted forces across six different models for test data

To verify the effectiveness and accuracy of our proposed rolling force prediction model on the test dataset, the rolling force predicted by the PSO-LSSVM-A model is compared with those predicted by the SVM, PSO-SVM, LSSVM, PSO-LSSVM, and LSSVM-A models, as well as sensor measurements. The results are presented in Fig. 12 and Table 3.

As shown in Fig. 12, while predicted values from all models generally follow the trend of the experimental values, there are notable differences in the accuracy and stability of rolling force predictions across models for different samples. The SVM model, in particular, exhibits higher error and instability, with its predicted rolling force values deviating more significantly from the experimental values.

The PSO-SVM model shows a slight improvement in rolling force prediction accuracy over the SVM model. Compared with both the SVM and PSO-SVM models, the LSSVM model achieves higher prediction accuracy and stability, displaying a better fit to the measured data. The PSO-LSSVM model further reduces prediction error and enhances stability compared with the LSSVM model, demonstrating the effectiveness of the PSO algorithm in improving rolling force prediction performance. The LSSVM-A model further enhances prediction accuracy over the LSSVM model alone, indicating the AdaBoost algorithm's effectiveness in boosting model accuracy. The PSO-LSSVM-A model achieves the highest accuracy, surpassing that of the LSSVM-A model.

To more clearly compare the difference in rolling force prediction accuracy between the model proposed in this study and the other models, we have zoomed in on specific sections in

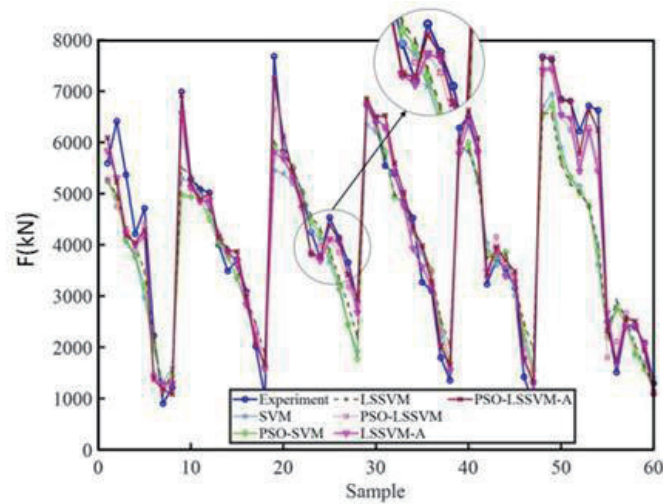


Fig. 12. (Color online) Comparison between predicted and measured rolling forces across different prediction models.

Table 3  
Performance evaluation of six force prediction models.

Model/Index	$R^2$		$MAE$		$RMSE$	
	Training	Test	Training	Test	Training	Test
SVM	0.808	0.799	591.417	635.762	799.597	870.935
PSO-SVM	0.833	0.807	558.797	623.958	746.669	852.851
LSSVM	0.825	0.865	604.363	597.813	764.779	817.225
PSO-LSSVM	0.971	0.938	231.990	374.780	309.439	484.353
LSSVM-A	0.985	0.942	158.644	329.047	220.492	469.841
PSO-LSSVM-A	0.994	0.963	92.730	267.674	136.125	373.025

Fig. 12. As shown in the circled areas, the predicted data from the PSO-LSSVM-A model (red line) is closest to the measured data (blue line), whereas the predicted data from the other models is less accurate, with the LSSVM-A model providing the best results among them.

The average errors for the rolling force prediction models SVM, PSO-SVM, LSSVM, PSO-LSSVM, LSSVM-A, and PSO-LSSVM-A are 17.74, 17.63, 6.67, 12.76, 9.76, and 8.72%, respectively. From the comparison plot of the model prediction results, it is evident that the PSO-LSSVM-A model consistently maintains high accuracy and stability, particularly at extreme points where the rolling force fluctuates significantly, demonstrating its excellent robustness.

From the comparison of data listed in Table 3, we find the following:

- (1) The SVM model exhibits relatively high  $MAE$  and  $RMSE$  values on both the training and test datasets, indicating its poor predictive validity compared with other models.
- (2) The PSO-SVM model demonstrates improved performance, with lower  $MAE$  and  $RMSE$  values on both the training and test sets relative to SVM.
- (3) The LSSVM model achieves similar  $MAE$  and  $RMSE$  values to PSO-SVM on the training dataset but performs slightly differently on the test dataset.
- (4) The PSO-LSSVM model significantly improves upon LSSVM, with much lower  $MAE$  and  $RMSE$  values on the training dataset. However, its predictive accuracy still needs

improvement at certain data fluctuation points, suggesting that further refinement is necessary.

- (5) The LSSVM-A model has lower *MAE* and *RMSE* values on the training dataset compared with LSSVM and PSO-LSSVM, indicating that the AdaBoost algorithm effectively enhances LSSVM's performance.
- (6) When comparing the *MAE*, *RMSE*, and  $R^2$  metrics, our proposed PSO-LSSVM-A model achieves optimal prediction accuracy, with  $R^2$  values of 0.99 and 0.96 on the training and test datasets, *MAE* values of 92.73 and 267.674, and *RMSE* values of 136.125 and 373.025, respectively. Despite increased error between predicted and measured values on the test dataset, the proposed PSO-LSSVM-A model demonstrates more stable and reliable performance than other models.

## 5. Conclusion

To address the issue of H-shaped steel damage caused by inaccuracies in traditional empirically based models for predicting rolling force in H-shaped steel hot rolling and web finishing, we proposed an innovative PSO-LSSVM-A rolling force prediction model. First, a comprehensive measurement system using multiple sensors was developed to capture 21 relevant parameter changes in the H-shaped steel before and after rolling. Next, the IForest algorithm was employed to remove outliers, effectively eliminating extreme rolling force fluctuations caused by environmental changes, mill vibration, and other factors, thereby enhancing model prediction accuracy. PSO was then used to fine-tune the parameters of the LSSVM model, and an adaptive weight allocation mechanism of the AdaBoost algorithm was applied to further improve the model's accuracy and robustness.

Our proposed PSO-LSSVM-A rolling force prediction model demonstrates the highest prediction accuracy among the models evaluated, particularly in handling data fluctuations caused by mill vibration and environmental changes, as well as in predicting the rolling force for new H-shaped steel specifications. This model significantly enhances yield and product quality across various H-shaped steel specifications.

To further improve prediction accuracy and reduce error, we will continue refining the feature parameters and optimizing the existing model, providing stronger support for industrial production.

## Acknowledgments

This work was supported by the Project of the Department of Science and Technology of Fujian Province, China (2022HZ026025, 2023T5001), the Program for Innovative Research Team in Science and Technology in Fujian Province University, and Fujian Provincial Engineering Research Center for Modern Mechanical Design and Manufacturing Technology, and in part by the Sanming University of Fujian Province, China (19YG05 and 19YG04).

## References

- 1 W. Zhang, C. Zhu, and G. E. O. Widera: *J. Mater. Process. Technol.* **56** (1996) 820. [https://doi.org/10.1016/0924-0136\(95\)01895-6](https://doi.org/10.1016/0924-0136(95)01895-6)
- 2 D. L. Shvarts and S. O. Nepryakhin: *Solid State Phenom.* **299** (2020) 546. <https://doi.org/10.4028/www.scientific.net/ssp.299.546>
- 3 S. O. Nepryakhin, V. A. Shilov, and D. L. Shvarts: *Steel Transl.* **44** (2014) 842. <https://doi.org/10.3103/S0967091214110138>
- 4 D. L. Shvarts and S. O. Nepryakhin: *Mater. Sci. Forum* **989** (2020) 622. <https://doi.org/10.4028/www.scientific.net/msf.989.622>
- 5 S. O. Nepryakhin, V. A. Shilov, and D. L. Shvarts: *Steel Transl.* **44** (2014) 842. <https://doi.org/10.3103/S0967091214110138>
- 6 X. Xu, Z. Baofeng, and Z. Mingyu: *J. Constr. Steel Res.* **182** (2021) 106682. <https://doi.org/10.1016/j.jcsr.2021.106682.C>
- 7 W. Q. Yang, Z. T. Zhao, L. Y. Zhu, X. Y. Gao, and L. Wang: *J. Iron. Steel Res. Int.* **31** (2024) 237. <https://doi.org/10.1007/s42243-023-01060-x>
- 8 Y. Dong, W. Zhang, and J. Song: *J. Iron Steel Res. Int.* **17** (2010) 27. [https://doi.org/10.1016/S1006-706X\(10\)60040-4](https://doi.org/10.1016/S1006-706X(10)60040-4)
- 9 Y. Dai, K. Roy, Z. Fang, G. M. Raftery, and J. B. Jim: *Proc. Cold-Formed Steel Research Consortium Colloquium* (2022) 17. <http://jhir.library.jhu.edu/handle/1774.2/67699>
- 10 O. Gamal, M. I. P. Mohamed, C. G. Patel, and H. Roth: *Int. J. Mech. Eng. Rob. Res.* **10** (2021) 349. <https://doi.org/10.1016/j.jmapro.2021.01.023>
- 11 A. A. Umanskii, A. B. Yur'ev, V. V. Dorofeev, and L. V. Dumova: *Steel Transl.* **51** (2021) 496. <https://doi.org/10.3103/S0967091221080155>
- 12 S. Nepriakhin: *Solid State Phenom.* **265** (2017) 1130 <https://doi.org/10.4028/www.scientific.net/ssp.265.1130>
- 13 R. Musab, P. V. F. Felipe, A. Ikram, L. Vireen, and S. Rabee: *Results Eng.* **17** (2023) 100902. <https://doi.org/10.1016/j.rineng.2023.100902>
- 14 J. Zhang, Y. Jing, Y., S. Chen, and D. Yang: *Eng. Fail. Anal.* **143** (2023) 106884. <https://doi.org/10.1016/j.engfailanal.2022.106884>
- 15 A. S. Elamary and I. B. Taha: *Materials* **14** (2021) 2364. <https://doi.org/10.3390/ma14092364>
- 16 A. P. de Oliveira, A. A. Gorni, and M. A. Rebellato: *Proc. 57th Rolling* **1** (2022) 1. <http://doi.org/10.5151/2594-5297-34162>
- 17 A. Pérez-Advarado, S. A. Arreola-Villa, I. Calderón-Ramos, R. Servín Castañeda, L. A. Mendoza de la Rosa, K. Chattopadhyay, and R. Morales: *Materials* **14** (2021) 7038. <https://doi.org/10.3390/ma14227038>
- 18 Y. Dai, K. Roy, Z. Fang, G. Raftery, and J. Lim: *Buildings* **13** (2023) 305. <https://doi.org/10.3390/buildings13020305>
- 19 J. S. Xia, K. M. Khaje, I. Patra, I. Khalid, A. J. Nuñez, A. Rahmanian, S. A. Eftekhari, and D. Toghraie: *ISA Trans.* **132** (2023) 353. <http://doi.org/10.1016/j.isatra.2022.06.009>
- 20 A. Müller, and A. Taras: *Proc. Annual Stability Conf. Structural Stability Res. Council Denver, Colorado, March* (2022) 22.
- 21 A. Hüseyin, M. O. İlhami, and E. İsmail: *Expert Syst. Appl.* **41** (2014) 7135. <https://doi.org/10.1016/j.eswa.2014.06.014>
- 22 K. Rajneesh, V. E. Parvathi, S. Aswin, V. Aswin, A. Anisha, P. J. Usman Arshad, M. Sujith, and D. Robin: *Struct.* **50** (2023) 1429. <https://doi.org/10.1016/j.istruc.2023.02.102>
- 23 M. S. Ahmad, S. M. Adnan, S. Zaidi, and P. Bhargava: *Constr. Build. Mater.* **248** (2020) 118475. <https://doi.org/10.1016/j.conbuildmat.2020.118475>
- 24 S. Dudenhausen, M. Waltering, and W. Kurz, W: *Proc. 40th IMAC, Proc. A Conf. and Expos. Structural Dynamics* **5** (2022) 69–79.
- 25 S. B. Su, Z. R. Zhai, C. S. Wang, and K. M. Ding: *Improved Fractional-Order PSO for PID Tuning. Int. J. Pattern Recognit. Artif. Intell.* **35** (2021) 1. <https://doi.org/10.1142/S0218001421590163>
- 26 V. N. Vapnik: *Proc. An Overview of Statistical Learning Theory in IEEE Transactions on Neural Networks* **10** (1999) 988. <http://doi.org/10.1109/72.788640>
- 27 J. Kennedy and R. Eberhart: *Proc. ICNN'95 Int. Conf. Neural Networks* **4** (1995) 1942. <https://doi.org/10.1109/ICNN.1995.488968>
- 28 S. Tsiapoki, O. Bahrami, M. W. Häckell, J. P. Lynch, and R. Rolfes: *J. Civ. Struct. Health Monit.* **20** (2020) 637. <https://doi.org/10.1177/1475921720909379>